Dome seeing monitor and its results for the 4-m Blanco telescope

Edison Bustos, Andrei Tokovinin

Cerro Tololo Inter-American Observatory, Casilla 603, La Serena, Chile

ABSTRACT

Optical distortions arising from inhomogeneous air in the telescope dome can be a non-negligible contributor to the delivered image quality (DIQ). Optimization of the dome environment is particularly important for first-class wide-angle imagers, such as the DECAM on the 4-m Blanco telescope, Omegacam at CFHT and, in the future, LSST. However, the standard method of comparing the DIQ with the site seeing does not single out the effect of the dome, being affected by contributions from other sources and by biases. We developed the dome seeing monitor for the Blanco telescope. It propagates the collimated 4-cm beam from the mirror cell to the top ring and back, parallel to the main beam. The angle-of-arrival fluctuations on this 10 m long path gives a quantitative estimate of the dome seeing. We describe the instrument and its software. The results for the Blanco telescope are presented. The median dome seeing is around $0.2''$. It shows the expected dependence on the temperature difference with the outside air and on the speed and direction of the wind.

Keywords: Site testing, turbulence, dome seeing, telescopes

1. INTRODUCTION

Despite advances in adaptive optics and space telescopes, modern astronomy needs seeing-limited ground-based imagery more than ever. Performance of wide-field instruments for imaging and spectroscopy, such as the Dark Energy Camera at CTIO, depends on the delivered image quality (DIQ) which, apart from the seeing, can be degraded by the optical aberrations of the telescope and instrument and by the internal seeing inside telescope enclosures. This latter factor, often called dome seeing, is difficult to quantify. Yet, reliable measurement of the dome seeing is needed to optimize dome ventilation and temperature control, trying to minimize the contribution of the dome seeing to the DIQ. Here we describe a simple device developed for this purpose, the *dome seeing monitor*. It is based on measuring the angle-of-arrival fluctuations of a narrow beam sampling a representative volume inside the dome (Fig. 1).

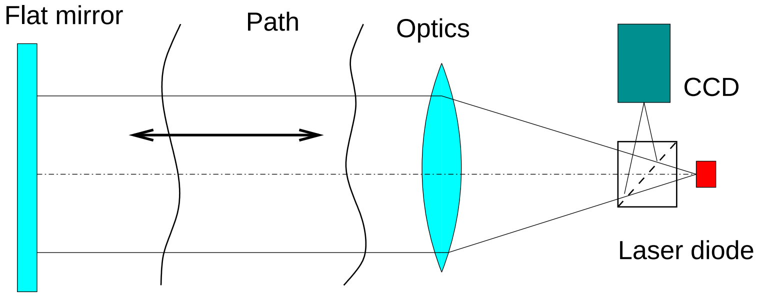

Figure 1. Idea of the dome seeing monitor. A collimated beam of light from a laser diode propagates inside the dome, is reflected back by a flat mirror, and focused by the same optics onto a CCD. The image motion produced by the turbulence is twice as large as for the single propagation.

In the early 1990s, with the advent of reliable data on atmospheric seeing furnished by the differential image motion monitors (DIMMs), astronomers realized that the DIQ of most telescopes was notably degraded by the dome seeing. Corrective measures, such as removal of heat sources from the domes and increasing the

---

E-mail: ebustos, atokovinin@ctio.noao.edu

ventilation, have been implemented and has led to a substantial improvement of the DIQ. However, as the dome seeing improved, the traditional method of evaluating it by comparing the DIQ with DIMM has became tricky because other factors contributing to the DIQ could not be quantified separately. Moreover, the seeing measured by DIMM is not necessarily representative of the seeing at the telescope. In a well-maintained telescope like Magellan, the DIQ is systematically better than the DIMM seeing.[4]

The need to measure the dome seeing reliably and independently of DIMM has been addressed using several approaches. When a SCIDAR instrument mounted on a telescope is used to measure the turbulence profile in the atmosphere, it can sense the seeing produced in the dome and in the telescope as a zero-wind turbulence at zero altitude.[1] Such turbulence can be measured using spatio-temporal correlation of the scintillation of a single bright star, as suggested by Shepherd et al.[7] Experiments in this direction are being conducted by V. Kornilov and his team at the 2.5-m telescope of the Sternberg Institute. On the other hand, real-time monitoring of the wave-front in any adaptive optics (AO) system can be used to extract the zero-velocity wave-front component by cross-correlation with a finite time lag. Dome seeing at Gemini-South was detected using the GEMS AO system telemetry by Guesalaga et al.[5]

However, most telescopes do not have AO systems or SCIDARs. An attempt to quantify dome seeing at the Keck telescopes using a commercial scintillometer has been made.[8] On the other hand, ESO initiated the LOTTUCE experiment involving multiple laser beams propagated inside the dome.[2] Its idea is to measure the phase structure function of turbulence inside dome, presumably different from the standard atmospheric models. The concept of structure function is, however, applicable to a stationary random process, whereas turbulence in the dome is expected to be non-stationary in both time and space. This problem is relevant to all methods of dome-seeing measurement, including the one presented here.

Here we propose to evaluate the dome seeing from the angular motion of a narrow beam that samples the optical path of the starlight (Fig. 1). Given the intrinsic inadequacy of the standard atmospheric theory inside telescope enclosures, this parameter can be related to the DIQ only approximately, as further discussed in § 2. Our simple instrument is described in § 3. Then in § 4 we give some results for the Blanco telescope. Our conclusions are given in § 5.

2. RELATION BETWEEN ANGULAR FLUCTUATIONS AND IMAGE BLUR

Optical distortions inside the dome are certainly neither homogeneous nor stationary. The standard atmospheric theory is therefore a poor approach from the outset. So, to what extent the angular jitter of a narrow beam can characterize the image blur in a large telescope?

In the framework of geometrical optics, the wave-front tilts by an rms angle σ produce a Gaussian blur with the same parameter σ. The FWHM ϵ of a Gaussian is larger than σ by a factor $f_{\rm Gauss} = \epsilon/\sigma = 2\sqrt{2 \ln 2} = 2.355$. Now, in the standard atmospheric model with infinite outer scale (i.e. Kolmogorov turbulence), the FWHM in an infinitely large telescope $\epsilon = 0.98\lambda/r_0$ is related to σ by the factor

$$f_{\rm Kolm} = \epsilon/\sigma = 2.354 (d/r_0)^{1/6}, \qquad (1)$$

where d is the diameter of the small beam and r_0 is the Fried parameter.[6] The factor f depends both on the turbulence strength and on the wavelength (through r_0). It is almost exactly equal to the Gaussian one when $d \approx r_0$. Thus, for a Kolmogorov turbulence the intuitive assumption that angle-of-arrival fluctuations of a narrow beam can be interpreted as a simple Gaussian blur in the large telescope is almost correct.

Although optical turbulence inside the dome is unlikely to conform to any model, we expect that the typical size of the distortions is less than the telescope diameter. Therefore, a stationary Von-Kármán (V-K) turbulence with a small outer scale L_0 can be used as a proxy to study the relation between angular fluctuations and image blur.

For a weak V-K turbulence, the phase structure function saturates, and the corresponding image blur kernel (PSF) contains a strong central peak, making calculation of the FWHM ϵ meaningless. To circumvent the problem, we assume that the PSF enlargement δ produced by the dome seeing is a quadratic contribution to the overall FWHM ϵ. In other words,

$$\delta = \sqrt{\epsilon^2_{\rm dome+atm} - \epsilon^2_{\rm atm}}. \qquad (2)$$

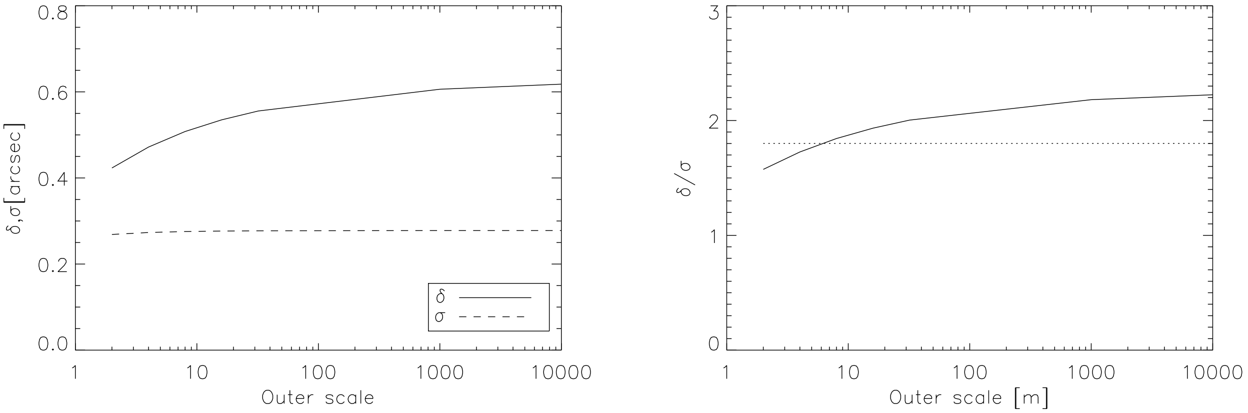

Figure 2. Contribution of the dome seeing to the image blur, δ, as a function of the outer scale L_0. Wavelength $\lambda = 0.5\mu$m, outside seeing $1''$, dome seeing $0.5''$ ($r_0 = 0.2\,$m). The left-hand plot shows the blur δ and the angular fluctuations of a 4-cm beam σ as a function of the outer scale L_0. The right-hand plot is their ratio, i.e. the factor f. For the Kolmogorov turbulence, $f_{\rm Kolm} = 1.80$ (horizontal dotted line).

This corresponds to the intuitive "Gaussian" definition of the image blur often assumed by astronomers.

Figure 2 shows representative results of our calculations. The outside seeing is assumed to be $1''$. The PSF produced by the combination of the external Kolmogorov turbulence with the V-K dome turbulence is computed numerically for the wavelength $\lambda = 0.5\mu$m. As we compute the difference between two similar values of ϵ, minor details matter. For this reason, the baseline FWHM $\epsilon_{\rm atm}$ is computed by the same numerical routine as used for computing the combined PSF, rather than analytically. In the right panel, we note that the factor $f = \delta/\sigma$ for large L_0 differs from its value given by eq. 1, owing to different definitions of the image blur (δ vs. ϵ).

If the turbulence in the dome resembles a V-K model with a small outer scale L_0, the factor f that converts the image motion measured by the dome probe into the FWHM blur is on the order of two, under a wide range of conditions. By adopting $f = 2$, the dome probe evaluates the image blur created by the dome seeing, to within $\sim$20%. At longer wavelengths, the blur will be systematically smaller, so by using $f = 2$ we might slightly over-estimate the dome seeing. As the image motion is doubled by double propagation, in the following we simply identify the measured rms scatter of the beam, σ, with the dome seeing FWHM blur.

All methods of measuring dome seeing rely on turbulence models. For example, scintillation measured by a SCIDAR or a scintillometer is interpreted using the Kolmogorov model. Non-stationary nature of optical distortions inside telescope enclosures necessarily implies an uncertainty in the interpretation of the results. Despite this uncertainty, the dome probe produces reliable *relative* measurements, allowing us to detect situations of poor dome seeing and to optimize the telescope enclosures.

3. THE INSTRUMENT

3.1 Opto-mechanical layout

The instrument is assembled from commercially available parts, with minimum additional custom mechanics. To shorten the size, we opted for the main lens of $F = 300\,$mm focal length with a focal extension by the negative (Barlow) lens, to the effective focal distance of $F = 1.8\,$m (Fig. 3). Given the 40-mm aperture d and the $\lambda = 635\,$nm wavelength, the radius of the Airy disc is $FD/\lambda = 28.6\,\mu$m, or 3.86 pixels per λ/d (the CCD pixel size is $7.4\,\mu$m or $0.85''$). The Airy spot is thus conveniently over-sampled, and the optics is diffraction-limited.

Most mechanical parts are procured from Thorlabs. The main lens (an achromatic doublet) is housed in a $2''$ diameter tube with a focuser. The back end is constructed from the $1''$ tubes and the beamsplitter with uncoated pellicle that transmits 92% of the light and reflects 8%. The return beam is reflected by the pellicle to the GC650 CCD camera made by Allied Vision, with its own focuser. A neutral density filter can be placed in

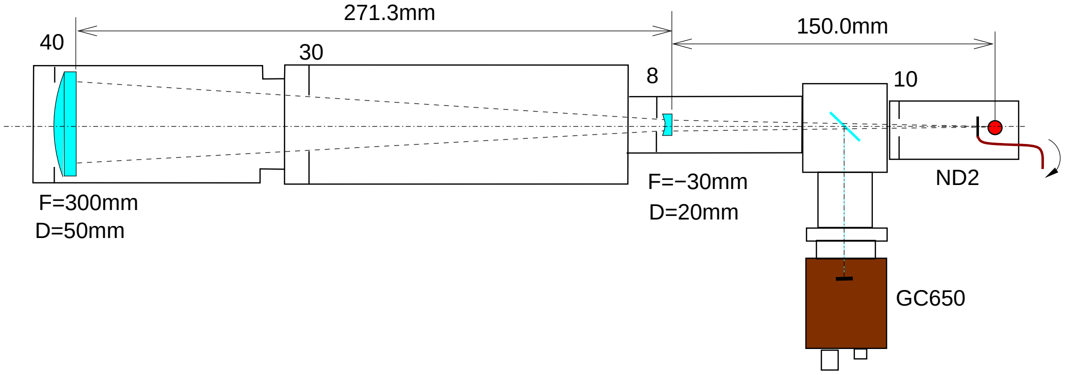

Figure 3. Layout of the dome probe instrument. The drawing is to scale.

the camera path to further dim the return light and avoid the saturation of the CCD. The 5 mW red (635 nm) laser diode is covered by a miniature filter with an optical density of 2. This filter can be manually flipped out of the beam for the initial adjustments and pointing, then inserted back for regular operation. This capability of having both bright and dim light is essential. The laser diode is fed by a 12 V power supply through a resistor of 330 Ohm, providing the current of 30 mA. Additional variable resistor of 2 kOhm in series serves to adjust the current, but it is by-passed during alignment to get maximum light.

As the instrument is used during regular telescope operation, it is essential to minimize the stray light. For this reason, the tube contains several circular stops (their locations and diameters are indicated in Fig. 3), preventing direct illumination of the inner tube walls by the laser diode. Indeed, very little light is seen when one looks into the tube from outside the main beam.

Collimated beam emerging from the tube is deflected by a flat 75-mm mirror in a kinematic mount adjustable in tilts. This mirror points the beam in the desired direction. The mirror mount was slightly modified to assure that the mirror is firmly pressed against three fixed points on the back side, rather than clamped at the edge. The first mirror can be omitted if, instead, we point the tube itself; however, it is more convenient mechanically to fix the tube. At the end of the propagation path, a second (identical) flat mirror reflects the beam back.

3.2 Computer and software

The signal from the Allied Prosilica GC-650 CCD GigE camera is acquired by the small fan-less PC computer from logicsupply.com. The computer has two Ethernet ports: one for the camera, another for the Local Area Network. It works under CentOS 7 Linux operating system.

The dome probe software `GUI_BDSP_v2.2.py` is written in python (Fig. 4). It uses the `Vimba` Allied Vision camera driver v2.1 and Pymba (a python wrapper for Vimba). When the program is started, it shows the full-frame images in real time, as needed for the initial centering of the source. In the measurement mode, only a small region of interest (ROI) around the spot is acquired, typically of 50×50 pixel size. The ROI size, exposure time, and frame rate are specified in the configuration file. A series of images is taken during a specified accumulation time (typically 30 s, also configurable). Spot positions in X and Y are computed as simple centroids for each frame. Each accumulation cycle begins by taking the full-frame image; the subsequent image sequence is centered on the spot position in this first image. In this way, the instrument can work unassisted without re-adjusting the pointing or the ROI location, as long as the spot is present in the full frame. After each accumulation period, the rms image motion in X and Y is computed and saved in the output text file together with other relevant parameters, such as universal time, spot position, flux, and maximum signal. A fragment of the data file is reproduced below.

```
UT_date    UT_time         Acc Texp  N_fr  Xcent   Ycent   Imax    Flux     rms_X rms_Y size mim
2018-02-03 22:49:32.558630 30 20000 1169 314.308 229.466 879.071 8591.548 0.186 0.227 26 27.295
2018-02-03 22:50:02.666547 30 20000 1174 312.309 231.255 880.228 8550.573 0.226 0.231 26 27.558
2018-02-03 22:50:32.764771 30 20000 1169 310.422 233.595 887.856 8548.961 0.254 0.323 25 27.704
```

The data are also displayed in the GUI. Optionally, one can display the centroid plots and their temporal spectra. Also optionally, sequences of individual centroid positions can be saved in binary format for off-line analysis.

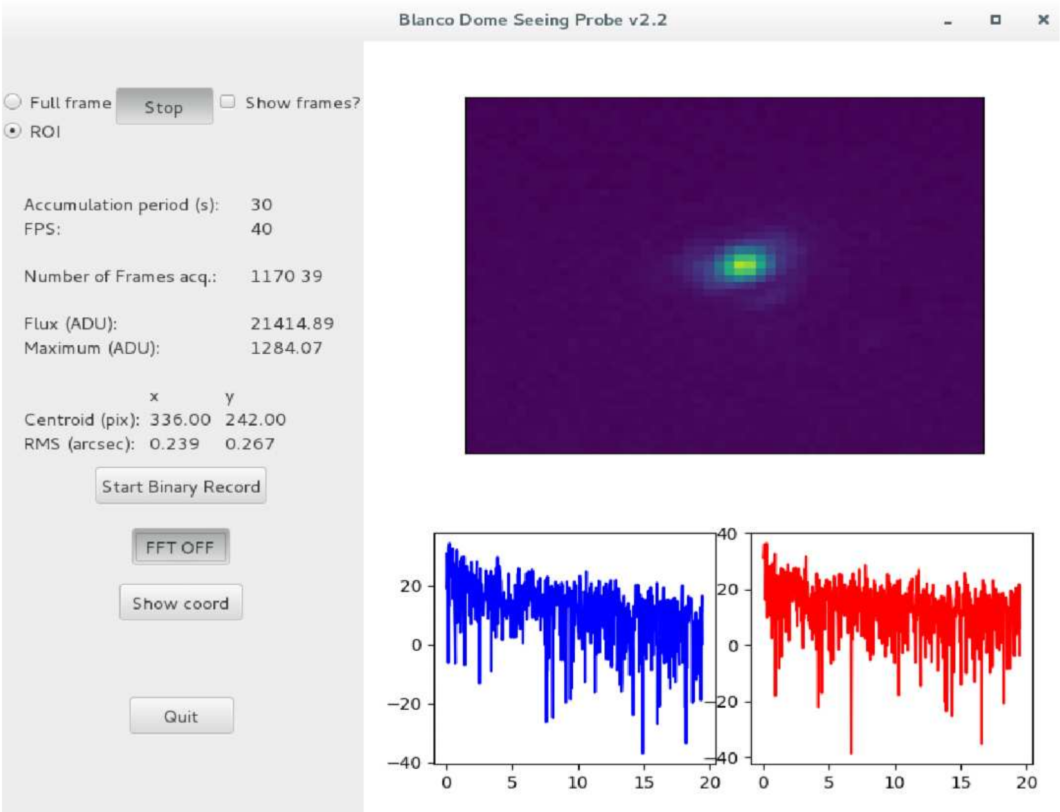

Accumulation period (s): 30
FPS: 40

Number of Frames acq.: 1170 39

Flux (ADU): 21414.89
Maximum (ADU): 1284.07

	x	y
Centroid (pix):	336.00	242.00
RMS (arcsec):	0.239	0.267

Figure 4. Screen-shot of the GUI. The left-hand portion shows the main acquisition parameters (accumulation time and frame rate), the actual number of frames acquired in the last accumulation period, the spot coordinates and their rms variance. Buttons control the options like saving binary data or displaying the spectra. The right-hand side shows the image (either live or just the first one) and the power spectra.

4. FIRST RESULTS

4.1 Initial tests

The instrument and its software were initially tested in the optical laboratory. In a stable situation, the individual centroids show an rms scatter as small at 10 mas, demonstrating the high intrinsic accuracy of the centroiding algorithm. The pixel scale was measured by tilting the tube in a controlled way and recording the spot position.

In May 2018, the instrument was installed for a few nights in the dome of the 1.5-m telescope at CTIO. The telescope was not used during this period. The propagation path of 3 m length was horizontal at $\sim$2 m height above the dome floor. The data were recorded continuously. Surprisingly, the largest rms spot motion of the order of $1''$ was recorded with closed dome during the night. Apparently, the dome is radiatively cooled at night, while the telescope and building are warmer, thus producing conditions for unstable convection inside the dome. In the daytime, the situation is reversed, the air stratification inside the dome is stable, and the spot motion can be as small as $0.1''$. When the dome was opened at night, the motion decreased to about $0.5''$. The power spectra of the centroids acquired at a rate of 100 Hz show the dominance of low ($<$10 Hz) frequencies and minor peaks at 20 Hz and 40 Hz caused by vibrations of the building.

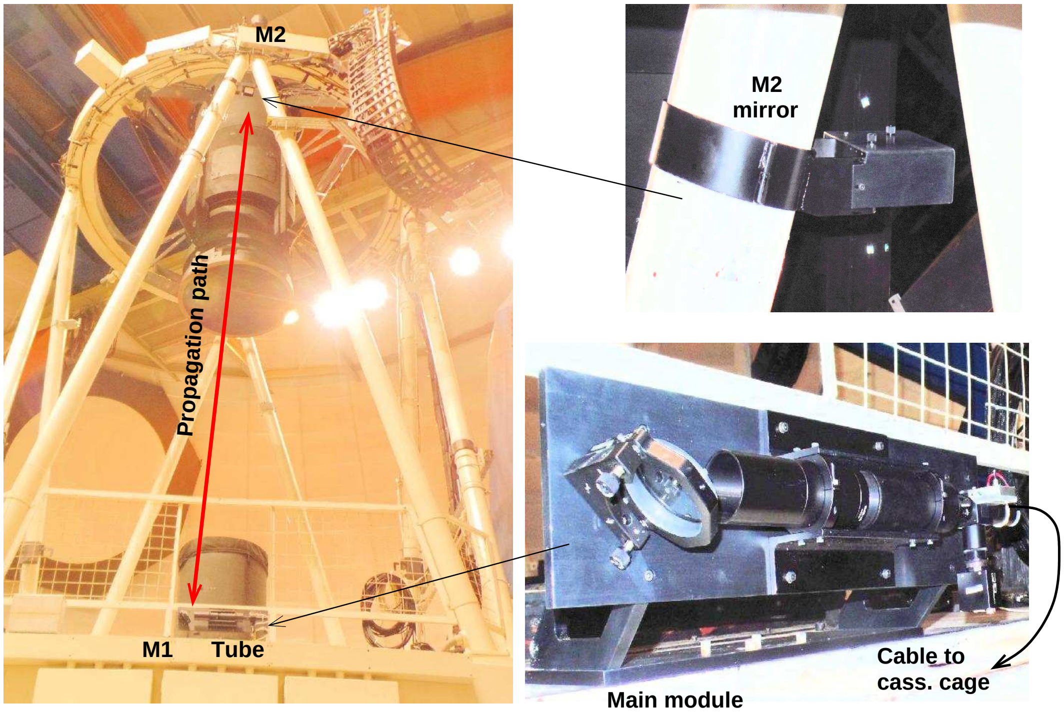

Figure 5. Dome probe installation at the Blanco telescope. The propagation path of 10 m length (left) is parallel to the telescope axis. The tube with the first mirror (lower-right) are attached to the mirror cell. The second mirror (top-right) is housed in a small open box clamped to the round white beam.

4.2 Installation at the Blanco telescope

The instrument was installed at the 4-m Blanco telescope located at Cerro Tololo in September 2017. The 10-m propagation path is parallel to the optical axis (Fig. 5). It starts at the edge of the mirror cell, where the tube and the first mirror are attached by means of an interface plate. The power and Ethernet cables are routed into the Cassegrain cage where the PC is housed. The power of the PC and the instrument is controlled remotely.

During installation, the mirrors must be adjusted. We adjust the tilts of the first mirror M1 to center the beam on M2, covered by a white paper. Then M2 is adjusted to return the beam to M1. After that, the adjustment is refined for spatial coincidence of the return and emitted beams. To do this, the outgoing beam is blocked by a paper with a 2-cm hole. The footprint of the return 2-cm beam on the paper can then be centered on this hole by slight tweaks of the M1 mirror. At this stage, physical access to M1 is no longer needed, so the telescope can point at the zenith. Finally, the spot is centered by looking at the live full-frame images. It is also important to regulate the laser current to avoid saturation of the CCD for the chosen exposure time.

We tested potential light contamination of the Dark Energy Camera, DECam[3] with the help of K. Vivas. On a cloudy night of October 22, 2017, she took two pairs of 300-s exposures in the r filter with the open dome and the telescope pointed to the white spot. One pair was taken with the dome probe light ON, another OFF. We looked at the signals of two CCDs located at the North and South edges of the field; both gave similar results, showing the absence of any background gradient in the N-S direction (the dome probe is installed on the northern side of the mirror cell). The average signal in 300-s exposures was 320 ADU, the increment due to the dome probe light was +3.7 ADU, or 0.012 ADU/s. The dome probe thus increases the light in the dark dome by 1.1%. The signal from the dark sky received in the r band is 2.8 ADU/s, so the relative increase of the sky background amounts to 0.4%. This is the upper limit because, very likely, the scattered laser light was reflected off the white spot; the actual contamination must be less when the telescope looks at the clear sky. After this test, the dome probe was left ON during normal telescope operation.

As the telescope points in different directions, the spot moves in the field owing to flexure. We tested this and found that the spot stays within 100 pixels from the center as the telescope moves off the meridian by ±2 h

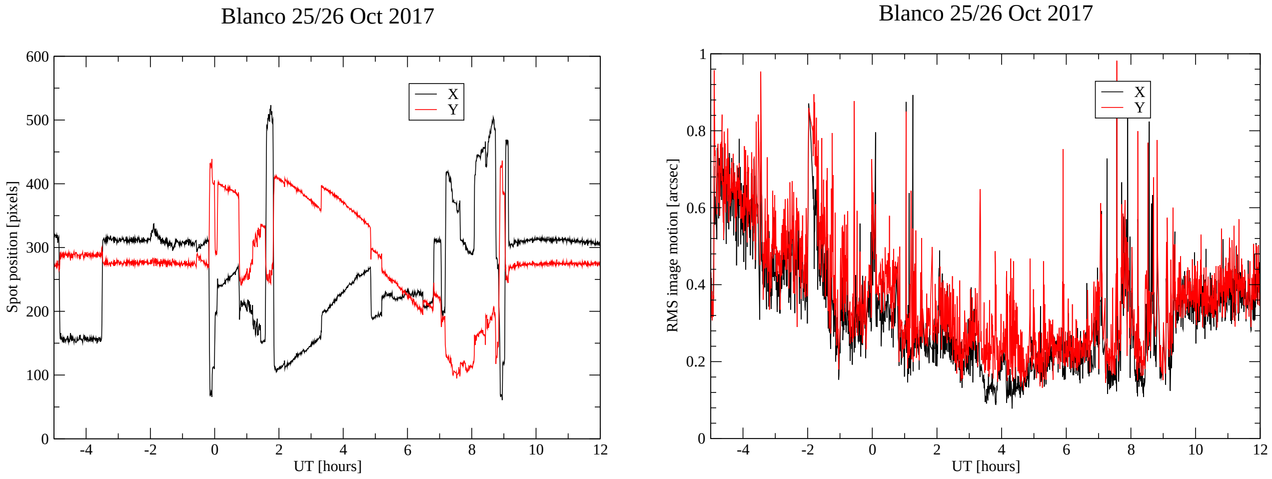

Figure 6. Dome probe results for the night of 2017 October 25/26. Left: spot position, right: rms spot motion.

in hour angle or points to the white spot (zenith distance 50°). The left panel of Fig. 6 shows spot coordinates during one typical night. In the evening, the telescope was pointed to the white spot for calibration, then to the zenith. During the night, the spot position reflects variable telescope pointing. In the plot of the rms spot motion (right panel), large rms values during telescope slews were filtered out, but some spikes still remain. The rms in Y is systematically larger than in X owing to the residual vibration (see below).

We collected the data continuously for several months without touching the instrument. However, the pointing had to be tuned again in 2018 January after the mirror wash procedure when, apparently, someone has moved the mirror. In 2018 February, the spot drifted again to the edge of the field, so valid measurements were obtained only for parts of the nights when the flexure did not move the spot outside the field.

The first data were acquired with a 100-Hz sampling frequency. The temporal spectra of the centroids had a strong vibrational component at ∼45 Hz, more prominent in the Y direction (N-S on the sky). To verify that this frequency is not an alias, we also took data with a faster frame rate of 200 Hz. This vibration contributed substantially to the total rms spot motion, unlike the situation at the 1.5-m telescope. As the expected signal from optical turbulence is concentrated at low frequencies, we increased the exposure time to 20 ms (effective frame rate 40 Hz, considering the readout overhead). The vibrations were effectively averaged out and the rms in X and Y became almost equal (Fig. 7). The remaining small systematic difference between the rms in X and Y is a sign of the vibration bias. This bias always increases σ.

4.3 One month of data

We explore here the data collected during the period from December 1, 2017 (0h UT) to December 28, 2017 (23:59 UT). The measurements were started at about 6 hours before the local midnight and terminated at 6 h after, thus sampling the night as well as the closed-dome periods. As the spot moves due to flexure when the telescope slews to different positions, the data were filtered by the criterion that the spot position does not change by more than 2 pixels compared to the previous and following data points (each data point is a 30-s accumulation). The filtering recovers 8319 valid measurements out of 39206 raw measurements. For 7987 of those, we also have the data from the telescope control system (TCS) and from the weather station.

Figure 8 shows the cumulative distributions of the rms spot motion σ in X and Y corresponding to the night-time operation (telescope tracking on) and daytime (no tracking). In both cases, the median values are quite small, around $0.2''$. However, there is a “tail” of larger σ during daytime. It corresponds to the morning hours when the dome air cooling system is turned on at the end of the night. The small systematic difference between X and Y reflects the residual vibration bias, affecting mostly Y.

In Fig. 9 we note some dependence of the dome seeing on the wind speed and direction. The best dome seeing corresponds to the wind speed between 10 and 15 m/s, when the dome is fully ventilated but the wind is

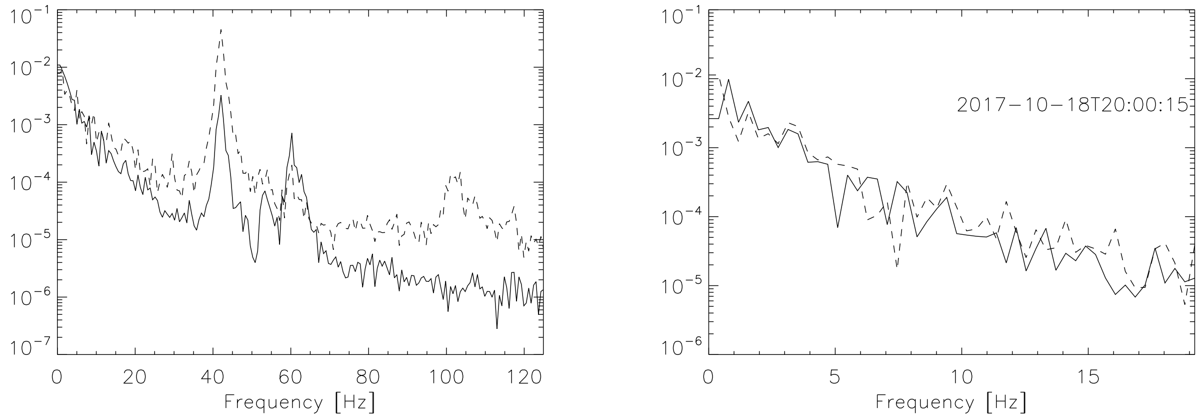

Figure 7. Power spectra of the centroid motion (full line – in X, dashed line – in Y). Left: acquisition on 2017-10-16 with a 5-ms exposure time showing the vibrations. Right: acquisition with a 20-ms exposure time on 2017-10-18.

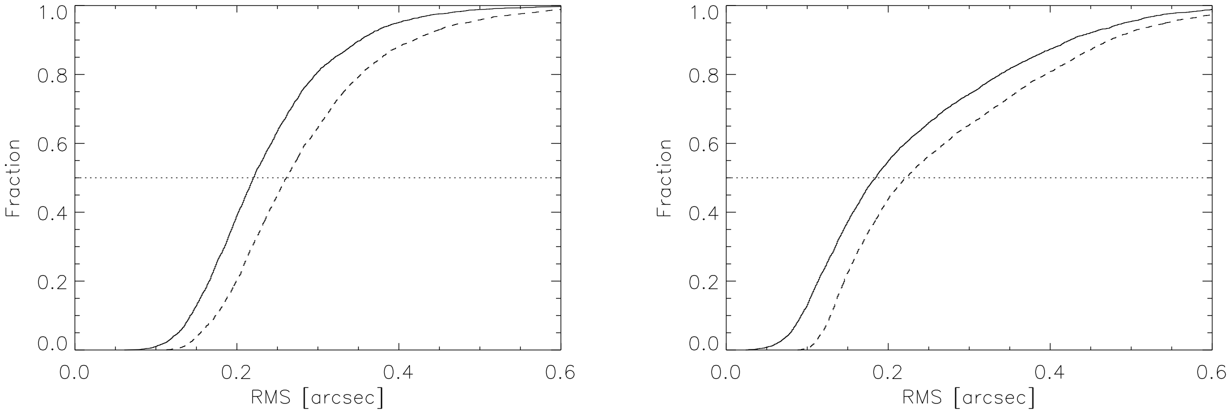

Figure 8. Cumulative histograms of the rms spot motion in X (full line) and in Y (dashed line). Left: 4030 data points when the telescope was tracking (night-time); medians 0.22″ and 0.26″ in X and Y, respectively. Right: remaining points (daytime), medians 0.18″ and 0.22″.

not yet too strong to create additional turbulence. The dome seeing degrades as the wind becomes slower. The wind direction *relative to the telescope and dome* seems to matter as well, because the best dome seeing happens when the wind is orthogonal to the telescope pointing.

Optical turbulence in the dome is expected to be proportional to the air temperature difference between inside and outside the dome. Indeed, Fig. 10 shows this effect, although the minimum occurs at a positive difference of +0.8°, rather than at zero. This bias is likely caused by the zero-point difference between the temperature sensors. One can deduce from this plot that the temperature inside the Blanco dome is controlled very well, as the difference rarely exceeds one degree. This explains why the typical dome seeing in the Blanco telescope is so good, around 0.2″.

We analyzed in the similar way the data collected in March–April 2018, when the ambient temperature was lower. Due to misalignment of the device, the data were collected only on parts of the night. The results are similar to those of December 2017. For example, the median night-time rms spot motion was 0.25″ in X and 0.30″ in Y. We will acquire data for at least one full year to sample all seasons.

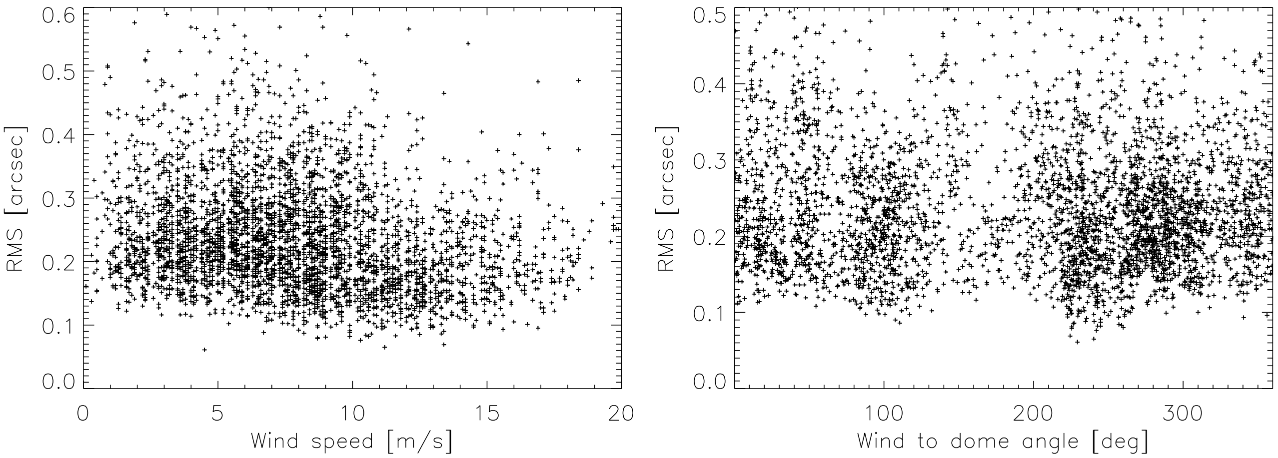

Figure 9. Dependence of night-time dome seeing on the wind speed in m/s (left) and on the wind direction relative to the telescope (right).

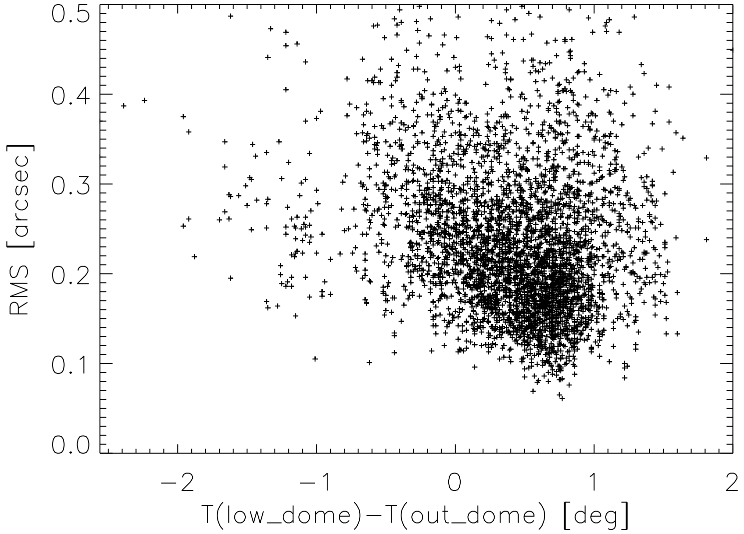

Figure 10. Dependence of night-time dome seeing on the temperature difference between inside and outside the dome.

5. CONCLUSIONS

We developed a simple device to measure angle-of-arrival fluctuations of a small beam propagated close to the telescope's main axis. It takes data in automatic regime on every night, not interfering with the normal telescope operation. The measured rms spot motion, doubled by the return propagation, can be interpreted as the approximate image blur caused by the dome seeing.

We found that the dome seeing in the Blanco telescope is generally very good, with a median value of $0.2''$. This is achieved by careful control of the dome environment (daytime cooling to keep the walls and telescope structure at or below the night-time temperature) and proper dome ventilation during the night. In most cases, the contribution of the dome seeing at Blanco to the overall DIQ is negligible. However, instances of dome seeing as large as $0.5''$ are also recorded, indicating that there is still some room for improvement. The optical path sampled by the dome probe does not include the dome slit; the mirror seeing is also not measured.

Figure 11 compares the DIQ in DECam with the DIMM seeing on two nights with calm atmosphere. Note that the DIQ is not corrected for the zenith distance and wavelength, while the DIMM seeing refers to zenith and to the wavelength of 500 nm. Unfortunately, during these nights the dome probe was misaligned and produced data only at the beginning of the night. It is obvious that the contribution of dome seeing to the DIQ is negligibly

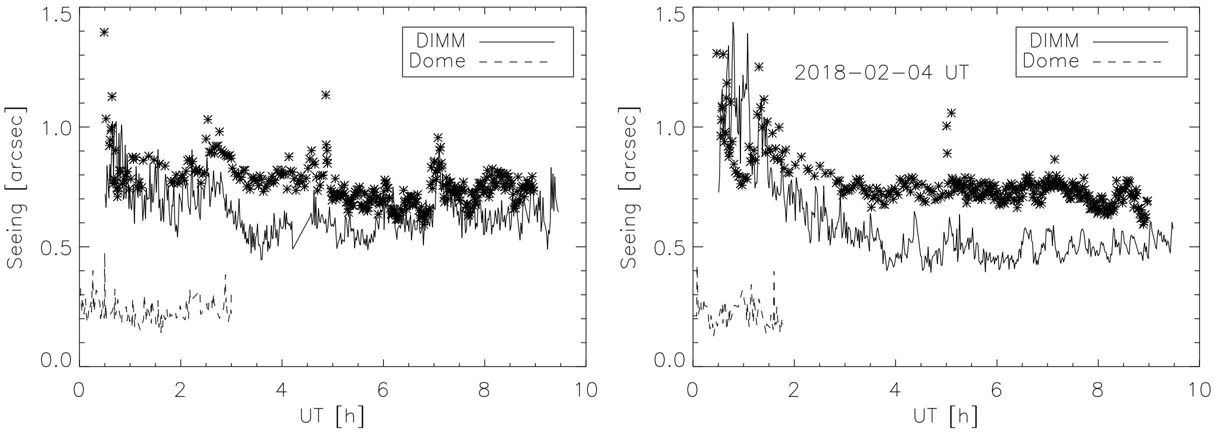

Figure 11. Comparison of the DIQ in Blanco DECam (asterisks), DIMM seeing (full line), and dome seeing (dashed line) on two nights with calm atmosphere: 2018 February 2/3 (left) and 2018 February 3/4 (right).

small. During the calm period of February 3/4 after UT 4h (see the right-hand plot), the median DIMM seeing was $0.49''$ and the median DIQ in DECam was $0.73''$. The quadratic difference of those values, $0.54''$, is a rough measure of all factors that enlarge the PSF compared to the seeing, such as dome seeing, optical aberrations, and charge spread in the CCD. The relative contribution of the dome seeing is small.

The dome seeing at Blanco appears to be better than in some other old classical telescopes. For example, a typical dome seeing of $0.6''$ at the CTIO 1.5-m telescope was documented in Ref. 1 during the Gemini SCIDAR site-testing campaign. Indeed, our brief tests with dome probe have shown a larger optical turbulence in this dome, presumably generated by the temperature difference with the outside air (the temperature is not actively controlled).

We foresee application of dome probe to other telescopes. It will help to optimize the temperature control and ventilation regime.

REFERENCES

[1] Avila, R., Vernin, J., Chun, M. R., Sanchez, L. J. “Turbulence and wind profiling with generalized scidar at Cerro Pachon, “ Proc. SPIE, 4007, 721 (2000)

[2] Berdja, A., Osborn, J., Sarazin, M.,Dali Ali, W., Ziad, A. “First results on dome probe turbulence characterization using the LOTTUCE prototype,”, Proc. AO4ELT3 Conf., DOI: 10.12839/AO4ELT3.13309 (2013)

[3] Flaugher, B., Diehl, H. T., Honscheid, K. et al. “The Dark Energy Camera,” AJ, 150, 150 (2015)

[4] Floyd, D. J. E., Thomas-Osip, J., Prieto, G. “Seeing, Wind, and Outer Scale Effects on Image Quality at the Magellan Telescopes,” PASP, 122, 731 (2010)

[5] Guesalaga, A., Neichel, B., Correia, C. et al. “Online estimation of atmospheric turbulence parameters and outer-scale profiling,” Proc. SPIE, 9909, 3C (2016)

[6] Roddier, F. “The effects of atmospheric turbulence in optical astronomy,”, in Progres in Optics, ed. E. Wolf, 19, 281 (1981)

[7] Shepherd, H. W., Osborn, J., Wilson, R. W. et al. “Stereo-SCIDAR: optical turbulence profiling with high sensitivity using a modified SCIDAR instrument,” MNRAS, 437, 3568 (2014)

[8] Vogiatzis, K., Otarola, A., Skidmore, W., Travouillon, T. Angeli, G. “Local thermal seeing modeling validation through observatory measurements,” Proc. SPIE 8449, doi:10.1117/12.927182 (2012)